Available online at www.sciencedirect.com
ScienceDirect
Trans. Nonferrous Met. Soc. China 30(2020) 559−570
Transactions of Nonferrous Metals Society of China
www.tnmsc.cn

Phase field lattice Boltzmann model for non-dendritic structure formation in aluminum alloy from LSPSF machine

An-shan YU[1,2], Xiang-jie YANG[1,2], Hong-min GUO[2,3]

1. School of Mechanical and Electrical Engineering, Nanchang University, Nanchang 330031, China;
2. Key Laboratory of Near Net Forming in Jiangxi Province, Nanchang 330031, China;
3. School of Materials Science and Engineering, Nanchang University, Nanchang 330031, China

Received 23 May 2019; accepted 23 December 2019

Abstract: The formation of non-dendritic structures in the primary phase of an aluminum alloy solidified using low superheat pouring with a shearing field (LSPSF) machine was investigated by numerical simulation. The growth and motion of a dendrite during solidification was simulated by a combination of the lattice Boltzmann method and the phase field method. The simulation results indicated that enough shear flow helped homogenize the concentration fields, rotate crystals and altere microstructures from dendritic to non-dendritic. The interaction of grains was also discussed. A fragmentation criterion was established based on partial remelting of dendrite arms; fragmentation was enhanced by a strong shear flow and larger inclined angles. The simulation results were verified experimentally.

Key words: numerical simulation; non-dendritic structure; low superheat pouring with shearing field (LSPSF); aluminum alloy; phase field method; lattice Boltzmann method

1 Introduction

Semisolid forming is a way for near net forming of wrought alloys due to the existence of non-dendritic solidification structures in semisolid slurry which effectively reduce or eliminate solidification shrinkage [1]. Therefore, efforts to understand non-dendritic structure formation under an external field have been made. Non-dendritic structure formation is a complex process which includes fluid flow, heat and mass transfer, complex coupling processes as well as crystal motion. These processes have significant research interest as well as industrial applications [2]. In the solidification process of low superheat pouring with a shearing field (LSPSF) [3], melt convection is primarily induced by rotation, pouring, density differences among different components, or temperature differences among different regions. Melt convection plays a key role in non-dendritic crystal growth, including low undercooling and increased nucleation. Grain movement in the melt significantly impacts the solidification process of an alloy; that movement also impacts microstructure and composition distribution during casting [4]. However, some of these mechanisms are still not very clear. For example, the mechanism of nucleus detachment and grain motion has limitations because direct observation of convection and motion during solidification is difficult; however, numerical modeling and simulation offer effective ways for studying such behavior.

Over the past 20 years, numerous solidification models have been developed for microscale analysis, such as phase field [5], cellular automata [6],

Foundation item: Project (51674144) supported by the National Natural Science Foundation of China; Project (KJLD14016) supported by the Luodi Research Plan of Jiangxi Educational Department, China; Projects (20122BAB206021, 20133ACB21003) supported by the Natural Science Foundation of Jiangxi Province, China; Project (20122BCB23001) supported by the Young Scientists Cultivating Program of Jiangxi Province, China
Corresponding author: Xiang-jie YANG; Tel:+86-15779293526; E-mail: yangxj@ncu.edu.cn
DOI: 10.1016/S1003-6326(20)65235-9

enthalpy [7] and level-set [8] methods. These models deal with the effect of the diffusive environment on dendrite growth and help explain heat and solute transport at the solid−liquid interface as well as understand factors that control the stability and shape of the dendrite tip [9]. Recent models have incorporated the effect of melt flow on dendrite growth. For example, large scale simulations have been carried out by coupling cellular automata using the lattice Boltzmann [10] and the phase field with the lattice Boltzmann method [11−13]. However, dendrite motion has been ignored in most models. To overcome this oversight, rigid body motion and rotation has been introduced in the growth of dendrites in alloys. LIU et al [14] used cellular automata−lattice Boltzmann to simulate the growth and motion of the equiaxed dendrites. MEDVEDEV et al [15] simulated a single dendrite solidification with motion and rotation with the phase field and lattice Boltzmann methods. ROJAS et al [2] and TAKAKI et al [16] used the phase field lattice Boltzmann method to simulate the growth and movement of a binary alloy. KARAGADDE et al [9] used a coupled volume of fluid (VOF)−immersed boundary method (IBM)−enthalpy method to simulate the growth and motion of equiaxed dendrites. TAKAKI et al [16] used a phase-field model coupled with Navier−Stokes equations to simulate dendritic growth and motion. Due to the accuracy of the phase field method and the easy parallel computation of the lattice Boltzmann method, we chose to use the phase field lattice Boltzmann method to simulate dendritic growth and motion.

Very few works have been published covering mesoscopic simulation of microstructure evolution during LSPSF rheoprocessing of Al alloys. The present study was focused on the investigation of non-dendritic structure formations of an aluminum alloy using LSPSF. The phase field lattice Boltzmann model was used initially to simulate dendritic growth and motion under rotation and gravity. The mechanism of non-dendritic structure formation based on simulation results is then discussed. Finally, the simulation results were verified experimentally.

2 Model description

The phase field lattice Boltzmann method originates from a combination of the quantitative phase field model for alloy solidification and the lattice Boltzmann method for fluid flow. For the quantitative phase field model, computing dendritic growth by treating the interface thickness is appropriate and the lattice Boltzmann method readily simulates fluid flow. For simplicity, the solid is assumed to be a rigid body and the net force exerted on the solid by fluid flow and other fields induces dendrite motion.

2.1 Phase field method

KARMA [17] and ECHEBARRIA et al [18] proposed the phase field model for alloy solidification. In this model, the phase field parameter φ indicates the phase distribution: +1 for solid and −1 for liquid. The time evolution of φ is given by

$$\tau(\theta)[1+(1-k)u]\frac{\partial\varphi}{\partial t}=\varphi(1-\varphi)^2-\lambda(1-\varphi^2)^2\cdot (u+\theta_{\text{sys}})(1+\dot{\zeta})+\nabla\cdot\{[W(\theta)]^2\nabla\varphi\}-\frac{\partial}{\partial x}[W(\theta)W'(\theta)\frac{\partial\varphi}{\partial y}]+\frac{\partial}{\partial y}[W(\theta)W'(\theta)\frac{\partial\varphi}{\partial x}] \quad (1)$$

where $\tau(\theta)$ represents the u-dependent phase field relaxation time, θ is the angle between the direction normal to the interface and a reference axis, k is the partition coefficient, φ is the phase field parameter, ζ is the noise term, λ is a dimensionless coupling constant that controls the coupling between the phase field and the concentration field, $W(\theta)$ is the interface thickness, $W'(\theta)$ denotes the derivative of $W(\theta)$ with respect to θ, u is the non-dimensional super-saturation, and θ_{sys} refers to non-dimensional temperature and $W(\theta)=W_0\cdot\alpha(\theta)$, $\tau(\theta)=\tau_0\cdot\alpha^2(\theta)$. The anisotropic function was set to be $\alpha(\theta)=1+\varepsilon_4\cos(4(\theta+\beta_0))$, where ε_4 is the anisotropic strength and β_0 is the orientation of the nucleus. For this simulation, $\varepsilon_4=0.04$, $W_0=d_0\cdot\lambda/\alpha_1$, $\tau_0=\alpha_2\cdot\lambda\cdot W_0^2/D$, where $\alpha_1=0.8829$, $\alpha_2=0.6267$ and d_0 is the chemical capillary length. To mimic system solute fluctuations, a single noise term ζ was introduced in Eq. (1) and realized using a Gaussian random number (zero mean) with specific amplitude (10^{-3}). Incorporating flow, the change of u as a function of time is expressed as

$$\left(\frac{1+k}{2}-\frac{1-k}{2}\varphi\right)\left(\frac{\partial u}{\partial t}+\boldsymbol{U}\cdot\nabla u\right)=\nabla\left(D\frac{1-\varphi}{2}\nabla u+J_{\text{AT}}\right)+\frac{1}{2}\frac{\partial\varphi}{\partial t}[1+(1-k)u] \quad (2)$$

The non-dimensional, super-saturation u and the anti-trapping J_{AT} are defined as

$$u=\frac{1}{1-k}\left[\frac{2c/c_1^0}{1+k-(1-k)\phi}-1\right] \tag{3}$$

$$J_{AT}=\frac{1}{2\sqrt{2}}[1+(1-k)u]\frac{\partial\varphi}{\partial t}\frac{\nabla\varphi}{|\nabla\varphi|} \tag{4}$$

where $k=c_\infty/c_1^0$, $D(=D_l\tau_0/W_0^2)$ is the dimensionless diffusion coefficient in a liquid; k is the partition coefficient; c_∞ and c_1^0 are the mean concentration and the solid−liquid interface concentration, respectively.

2.2 Lattice Boltzmann method (LBM)

The lattice Boltzmann method was used to calculate the fluid velocity to simulate fluid flow. In the two-dimensional nine velocity (D2Q9) model used here, the evolution of a single relaxation time τ and the discrete forcing term G_i in the lattice Boltzmann method are expressed as

$$f_i(\boldsymbol{x}+\boldsymbol{c}_i\delta t,\ t+\delta t)=f_i(\boldsymbol{x}+t)-\frac{1}{\tau}[f_i(\boldsymbol{x},t)-f_i^{eq}(\boldsymbol{x},t)]+G_i(\boldsymbol{x},t)\delta t \tag{5}$$

where f_i is the fluid distribution function for a particle moving with a discrete velocity $\boldsymbol{c}_i$ at time t and at position $\boldsymbol{x}$.

The discrete velocity set $\{\boldsymbol{c}_i|i=0,\ 1,\ \cdots,\ 8\}$ in the D2Q9 model is

$$\boldsymbol{c}_i=\begin{cases}0,\ i=0\\(\cos[(i-1)\pi/2],\ \sin[(i-1)\pi/2])c,\ i=1,\ 2,\ 3,\ 4\\\sqrt{2}(\cos[(i-5)\pi/2+\pi/4],\ \sin[(i-5)\pi/2+\pi/4])c,\\\quad i=5,\ 6,\ 7,\ 8\end{cases} \tag{6}$$

where $c=\delta x/\delta t$ is the lattice speed, δx is the lattice cell width and δt is the time step. To match Δx and Δt from the phase field method, it was necessary to rescale δx and δt to 1 in LBM computations. The density ρ and velocity U of the fluid were determined by

$$\rho=\sum_{i=0}^{Q-1}f_i \tag{7}$$

$$\rho\boldsymbol{U}=\sum_{i=0}^{Q-1}\boldsymbol{c}_i f_i \tag{8}$$

The equilibrium distribution function f_i^{eq} was defined using the fluid density and velocity as

$$f_i^{eq}=w_i\rho[1+\frac{3(\boldsymbol{c}_i\cdot\boldsymbol{U})}{c^2}+\frac{9(\boldsymbol{c}_i\cdot\boldsymbol{U})^2}{2c^4}-\frac{3\boldsymbol{U}\cdot\boldsymbol{U}}{2c^2}] \tag{9}$$

The weighting factor, w_i, differs as a function of i, w_0=4/9, w_{1-4}=1/9, w_{5-8}=1/36 and the fluid viscosity is calculated by $v=(\tau-1/2)\delta t\cdot c^2/3$. Tracking the exact interface position and implementing a non-slip boundary condition was more challenging than using sharp interface models. Considering this, the no-slip condition between the melt and the solid was realized via drag resistivity in the diffuse interface region. To satisfy the no-slip condition in the vicinity of the liquid−solid interface, the external force, G, was calculated as a second-order function using the equation below [19]:

$$G_i=w_i\rho\left[3\frac{\boldsymbol{c}_i-\boldsymbol{U}}{c^2}+9\frac{(\boldsymbol{c}_i\cdot\boldsymbol{U})\cdot\boldsymbol{c}_i}{2c^4}\right]\cdot\boldsymbol{G} \tag{10}$$

$$\boldsymbol{G}(x,t)=\frac{2\rho\nu h^*}{W_0^2}(\frac{1+\varphi}{2})^2(\boldsymbol{U}_s-\boldsymbol{U}) \tag{11}$$

where h^* is a dimensionless constant (h^*=2.757), W_0 is related to the interface thickness and U_s is the solid velocity.

2.3 Solid motion

According to Newtonian law, calculation of particle motion utilizes the following equations and an updated phase field, φ, by solving the advection equation [20,21]:

$$M_s\frac{d\boldsymbol{U}_T}{dt}=\boldsymbol{G}_s \tag{12}$$

$$\boldsymbol{I}_s\frac{d\omega_s}{dt}=\boldsymbol{T}_s \tag{13}$$

$$\boldsymbol{G}_s=-\sum_{x\in\Omega}\boldsymbol{G}(\boldsymbol{x},t)\Delta V+(1-\frac{\rho_l}{\rho_s})M_s g \tag{14}$$

$$\boldsymbol{T}_s=-\sum_{x\in\Omega}(\boldsymbol{x}-\boldsymbol{X}_s)\times\boldsymbol{G}(\boldsymbol{x},t)\Delta V \tag{15}$$

$$U_s=\boldsymbol{U}_T+\omega_s\times(\boldsymbol{x}-\boldsymbol{X}_s) \tag{16}$$

$$\frac{\partial\varphi}{\partial t}+\boldsymbol{U}_s\cdot\nabla\varphi=0 \tag{17}$$

where M_s and $\boldsymbol{I}_s$ are the mass and inertial tensors of the solid, $\boldsymbol{G}_s$ and $\boldsymbol{T}_s$ are the total force and torque acting on the solid, $\boldsymbol{U}_T$ and ω_s are the translational and angular velocities of the solid, ΔV and Ω are the volume of the computational lattice and the domain in the vicinity of the solid interface, ρ_l and ρ_s correspond to liquid and solid densities, respectively, g is the gravity constant and $\boldsymbol{X}_s$ is the center of mass of the solid.

The basic solution of the present model was

obtained as follows:

(1) Solve Eqs. (1)−(4) using the finite volume method.

(2) Solve the lattice Boltzmann equation and satisfy the no-slip boundary condition using Eqs. (5)−(11).

(3) Obtain U_s using Eqs. (12)−(16) and update the phase field location with Eq. (17). The advection equation was discretized with the WENO fifth-order scheme in space and the Runge−Kutta third-order scheme in time.

(4) The program was written using C++; data analysis and visualization were completed in MATLAB.

3 Experimental

In this study, aluminum alloy 6063 was used as the experimental material with an elemental composition of 0.68% Mg, 0.52% Si and 0.14% Fe, with the balance being aluminum. The liquid and solid temperatures of the alloy were 658 and 618 °C, respectively. In the experimental procedures, a LSPSF process was used to obtain the non-dendritic, α(Al) phase. The experimental equipment is shown in Fig. 1 and a detailed description of the LSPSF process and associated equipment can be found elsewhere [3]. The experimental parameters are given in Table 1. The alloy was initially melted in a clay-graphite crucible at 720 °C; when the melt reached a preset temperature, approximately 1.5 kg of the melt was poured into a rotating barrel at room temperature. The melt was collected in an accumulator at 650 °C. At the same time, sample slices were cooled rapidly with water for 15 s, properly polished and chemically etched with a 10% aqueous NaOH solution. Microstructures were observed using an optical microscope.

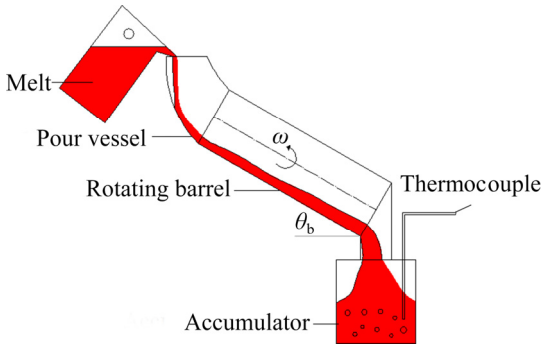

Fig. 1 Schematic illustration of LSPSF device used in experimental procedure

Table 1 Parameters used in LSPSF process

Pouring temperature/°C	Rotative velocity, ω/(rad·s^{-1})	Inclined angle, θ_b/(°)
670	1, 1.25, 1.5, 1.75, 2	15, 20, 25

4 Results and discussion

The motion and growth of grains in a binary alloy during solidification were established. An Al−Mg aluminum alloy system was selected for simulations, and its physical properties are listed in Table 2. All numerical simulations were dimensionless with $\Delta x/W_0$=0.4 and Δx=4.44×10^{-8} m, while the time step was Δt=7.0×10^{-8} s. The lengths and widths of the simulated domain were L_x=L_y=800Δx in the x and y directions. The initial diameter of the seed was D=10Δx. The dimensionless coupling parameter was λ=5.5. The density ratio, ρ_s/ρ_l, was 1.05 with gravity acting along the y axis. The non-dimensional super- saturation was u=−0.65. For isothermal conditions, θ_{sys}=0 since the use of the actual kinematic viscosity would be unrealistic to perform the simulation in a reasonable computation time. The relaxation time in the LBM, τ, was set to be 0.575. The computation was performed for 3×10^4 steps. The boundary conditions for φ and u were set as the zero Neumann condition for all boundaries. The non-equilibrium extrapolation scheme was adopted for the flow field boundary conditions and a no-slip boundary condition was applied to the solid boundary.

Table 2 Physical properties of Al−Mg aluminum alloy [22,23]

Parameter	Value
Initial mass fraction of alloy, c_0/%	0.68
Liquidus temperature, $T_{l,eq}$/K	933.47
Solute partition coefficient, k	0.32
Liquidus slope, k_l/(K·%$^{-1}$)	−5.07
Solute diffusion coefficient in liquid, D_l/(m^2·s^{-1})	3.0×10^{-9}
Gibbs−Thompson's coefficient, Γ/(K·m)	1.3×10^{-7}
Density, ρ/(kg·m^{-3})	2.36×10^3

4.1 Effects of rotative velocity on microstructure morphology

To investigate the influence of rotative velocity on dendritic growth and solute distribution, we

considered four different rotative velocities (ω): 0, 10, 20 and 40 rad/s. Initially, a solid seed was placed in the melt and a constant flow, ω, in a circumferential direction was applied on a radial axis from the domain center towards the outside. The boundary conditions for φ and u were set as the zero Neumann conditions for all boundaries. For the flow field, a no-slip condition was applied to the solid boundary. A non-equilibrium extrapolation scheme was adopted to treat the open boundary conditions.

Morphological changes and variations in the concentration fields are shown in Figs. 2 and 3. As the rotative velocity increased, the area of the dendrite decreased and the length of the dendrite arms became shorter. The dendrite tip interface concentration increased while the dendrite root interface decreased. As the rotative velocity increased, more solute was drawn from root to tip, which resulted in a more homogeneous concentration. Figure 3(a) indicates that larger rotative velocities corresponded to a wider distance between the tip interface and the bulk melt (δ). For diffusion-limited growth of a dendrite tip, the tip velocity (R) [24] satisfied $R=D_l/\delta$, where D_l corresponds to the diffusion coefficient. This implied that the tip velocity of the dendrite decreased as the rotative velocity increased; Fig. 3(b) also shows that the dendrite root interface concentration decreased as the rotative velocity increased. Thus, the dendritic arm roots grew faster and promoted stable non-dendritic structure growth. Therefore, the rotative shear flow effectively decreased the segregation in practice, while a non-dendritic structure phase was obtained using higher rotative velocities.

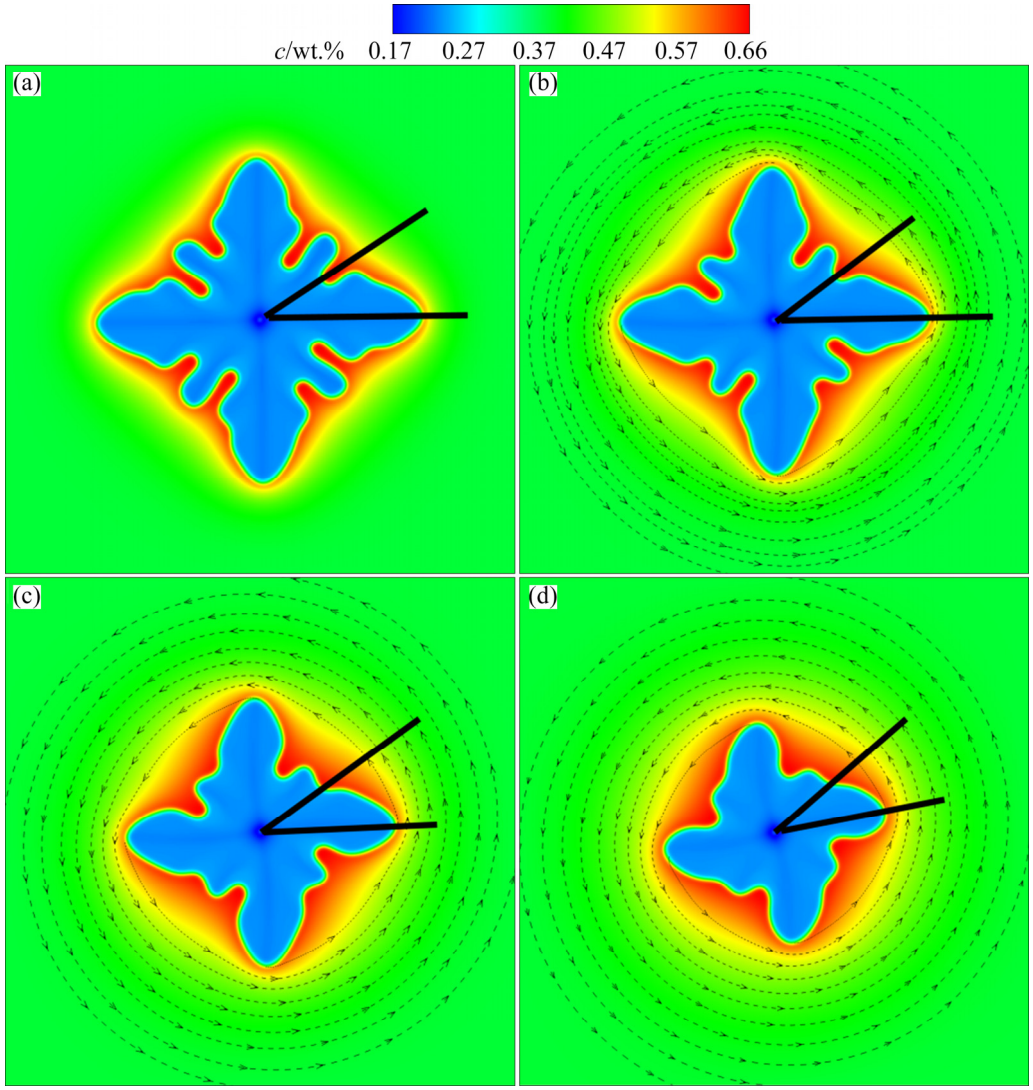

Fig. 2 Concentration distribution during dendritic growth at different rotative velocities: (a) 0 rad/s; (b) 10 rad/s; (c) 20 rad/s; (d) 40 rad/s

4.2 Effects of inclined angle on microstructure morphology

Different inclined angles (θ_b) were used to investigate the effect of incline angle on solidification microstructures. These different angles corresponded to different settling accelerations (S_A), given by $S_A=g\sin\theta_b$ (g is the gravity constant; S_A=2.539, 3.355 and 4.146 m/s^2). The morphological changes and the concentration field variations are shown in Figs. 4 and 5. As the settling acceleration increased and the dendrite fell, the four-fold growth was asymmetric. The downward directional growth velocity of the dendrite increased while high concentrations suppressed the upward direction growth velocity. The two parts of the left and right grew asymmetrically; therefore, slight dendrite rotation occurred. From Fig. 5, the solute released from the downward tip diffused rapidly; diffusion of side arms tip is the second and the diffusion of the upward tip was slow under the effect of the flow field. This led to a thin boundary layer at the end of the flow current and the thickness of the boundary layer at the back of the flow as well as asymmetry of dendrite growth. Figure 6 shows the settling velocity, V_s and the angular velocity of the dendrite, ω_s. The effect of gravity increased as the dendrite grew; therefore, the settling velocity and resistance of this dendrite also increased. As the resistance and gravity reached equilibrium, the settling velocity of the dendrite stabilized; a larger settling acceleration contributed to forced flow, which then induced a small angular velocity of the dendrite, as shown in Fig. 6(b). Since the angular velocity of the dendrite was small, this weakened the solute distribution; therefore, solute distribution was altered primarily by settling acceleration.

The solutions above assumed an initial dendrite nucleus orientation of β_0=0 rad. That is to say, one of the preferred growth axes of the dendrite occurred in the settling acceleration direction that resulted in a stable settling. That explains lower dendrite rotation in this case. The next simulation initially set β_0=0.785 rad; the non-zero growth

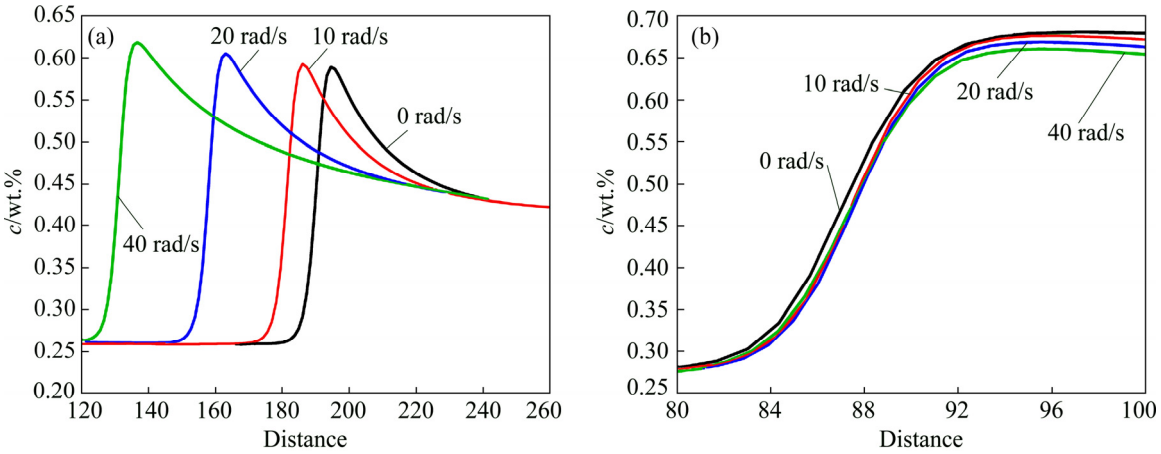

Fig. 3 Interface concentrations of tip (a) and root (b)

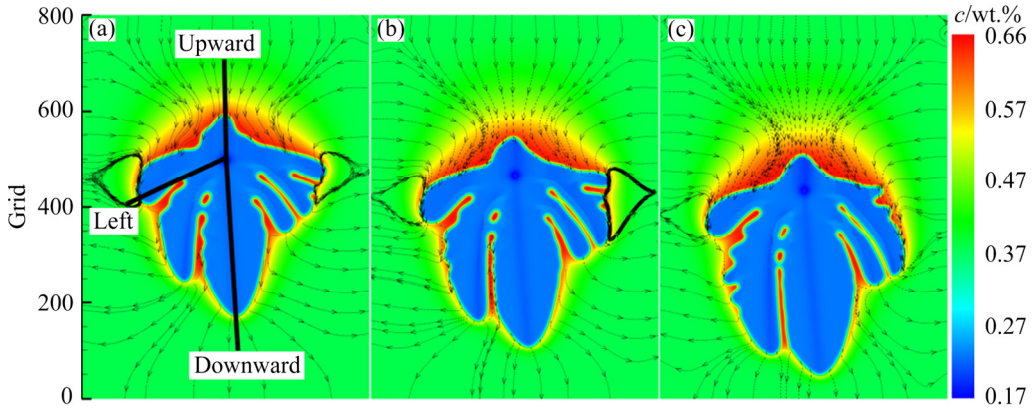

Fig. 4 Concentration distribution during dendrite growth under different settling accelerations, S_A, at initial dendrite nucleus orientation of β_0=0 rad: (a) 2.539 m/s^2; (b) 3.355 m/s^2; (c) 4.146 m/s^2

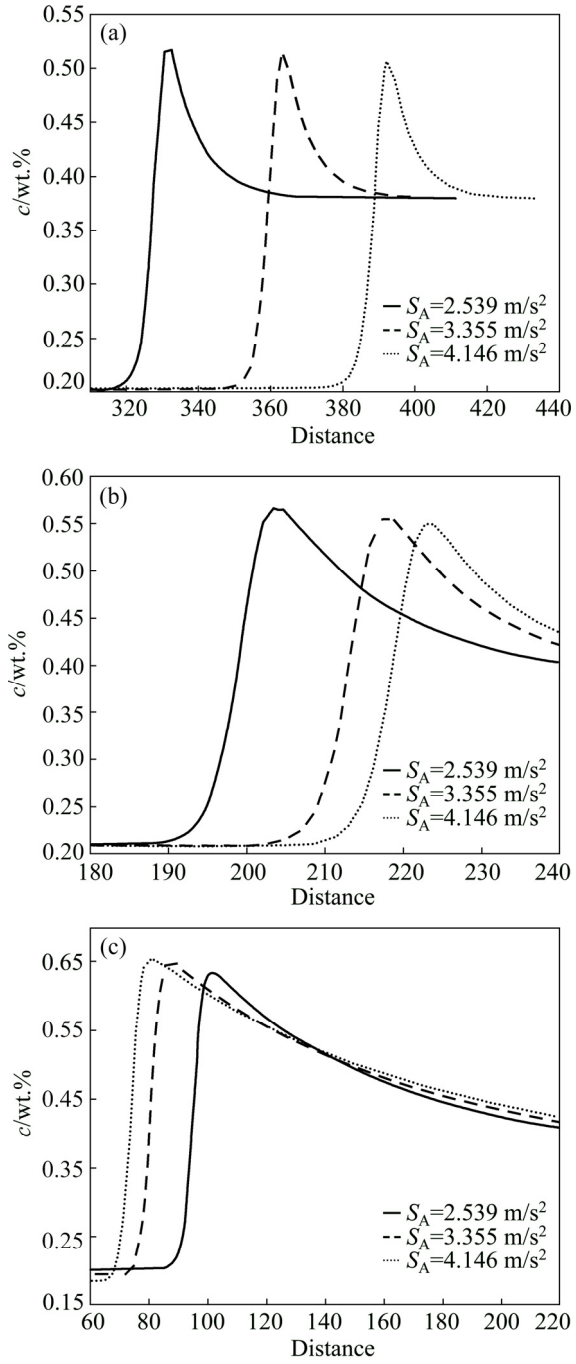

Fig. 5 Tip concentrations of downward (a), left (b) and upward (c) arms

orientation of the dendritic branches resulted in asymmetric growth (Fig. 7). Conclusions from other groups [25] suggested that different velocities of the growing branches depended on the local flow surrounding each tip. When the shape of the dendrite became asymmetrical, it readily rotated in search of other stable orientations. The evolution of the settling velocity and angular velocity of the dendrite falling at different settling accelerations

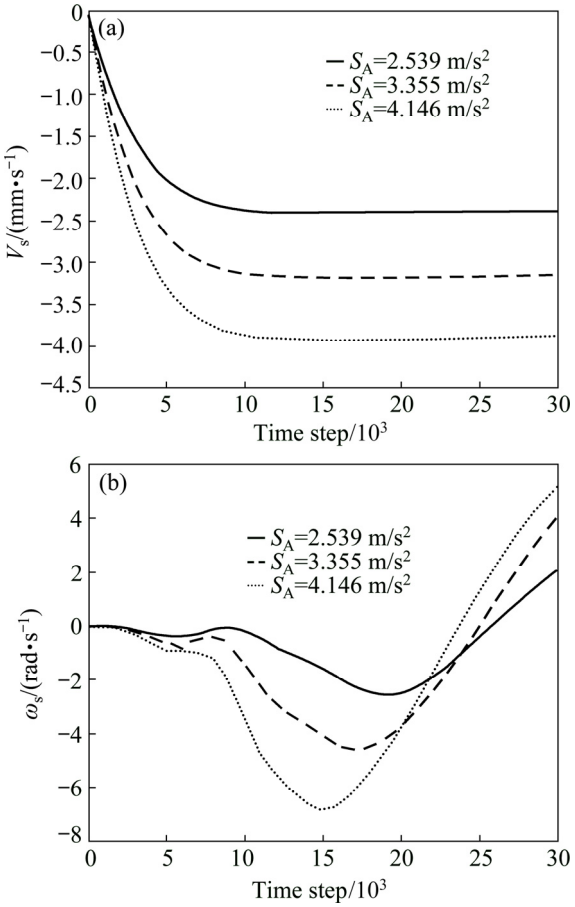

Fig. 6 Variations of settling velocity, V_s (a) and angular velocity, ω_s (b), for three different settling accelerations at initial dendrite nucleus orientation of β_0=0 rad

is shown in Fig. 8. Figures 6 and 8 demonstrate that when S_A=4.146 m/s^2, the angular velocity of the dendrite (at β_0=0.785 rad) was four times faster than for β_0=0 rad and nearly twice as fast when S_A= 2.539 m/s^2. This indicated the larger settling acceleration and orientation of the dendrite in space both induced dendrite rotation. Thus, the orientation of the dendrite in space and melt flow codetermine dendrite shape and growth direction.

4.3 Grain interactions

To investigate the interaction effect of different grains on their morphology and growth kinetics, a calculation domain with five seeds was used and the results are shown in Fig. 9. The simulation only included overlapping of the solute diffusion, and others were ignored. The Mg concentration gradient in the liquid rapidly dropped due to diffusion layer overlap around the grains (Fig. 9(b)). As a result, dendritic tip growth was inhibited. While larger Mg concentration variations were observed in the liquid

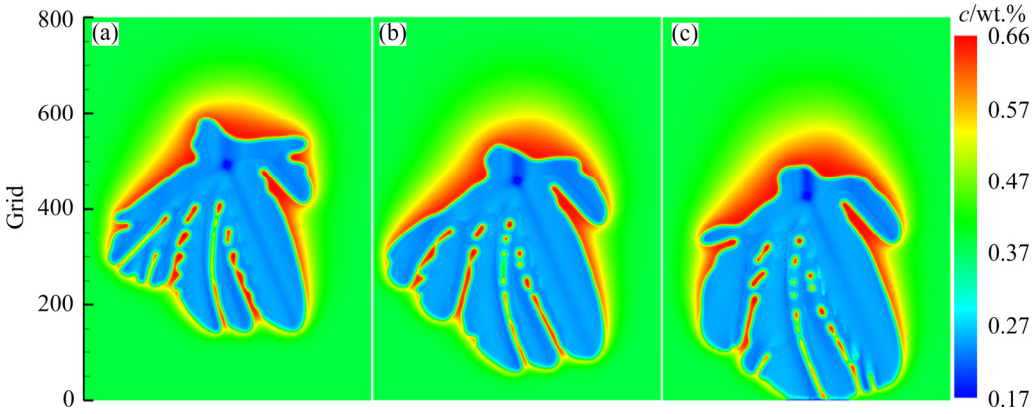

Fig. 7 Concentration distribution during dendrite growth under different settling accelerations, S_A, at initial dendrite nucleus orientation of β_0=0.785 rad: (a) 2.539 m/s^2; (b) 3.355 m/s^2; (c) 4.146 m/s^2

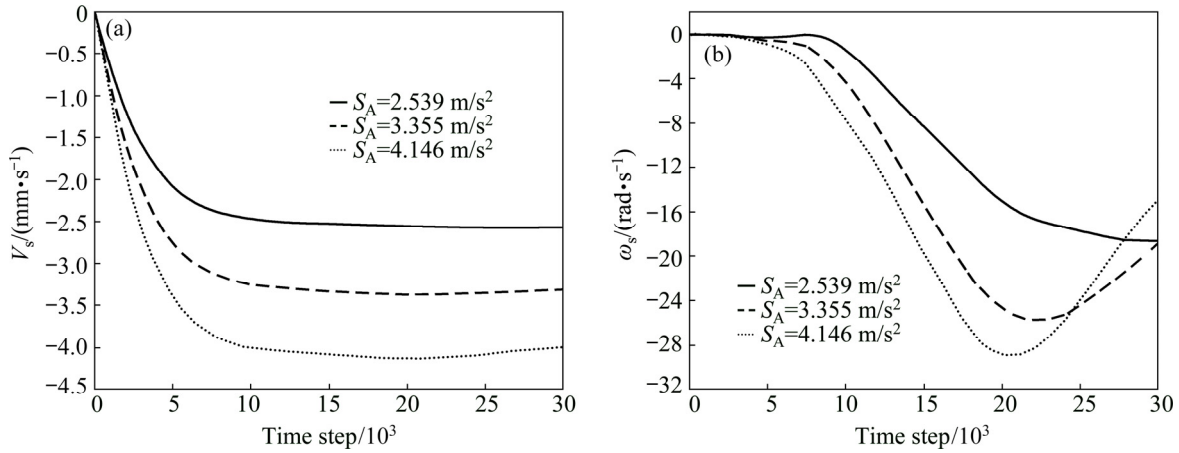

Fig. 8 Variations of settling velocity, V_s (a), and angular velocity, ω_s (b), for three different settling accelerations at initial dendrite nucleus orientation of β_0=0.785 rad

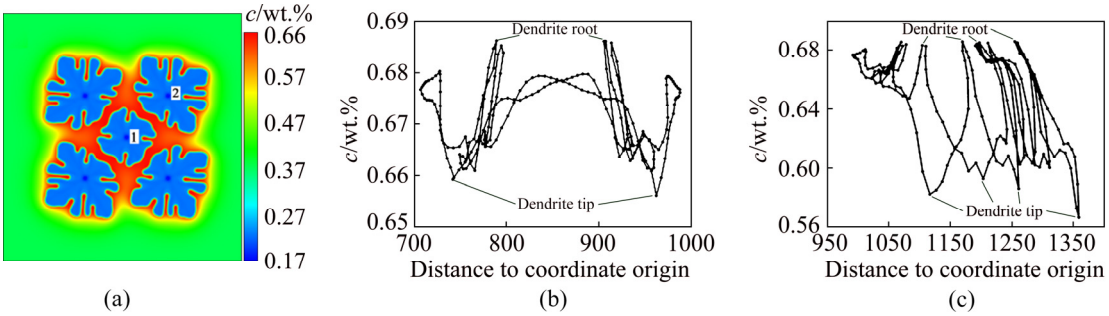

Fig. 9 Effects of grain interactions on growth morphologies and Mg concentration field around grains (a), and Mg concentration distribution curves in melt ahead of solid−liquid interface of Grain 1 (b) and Grain 2 (c)

(Fig. 9(c)), this situation led to a destabilization of the solid–liquid interface and a free dendritic arm morphology. Figure 9(a) shows few secondary arms due to the overlap of diffusion layers around the grains. Therefore, overlapping of the solute diffusion layers around the grains opposed the applied driving force [24,26], which is, in practice, reduced to the dendrite tip effective undercooling. The interface stability and the interface energy were also enhanced; the solute distribution over the solid−liquid interface was more uniform and the dendrite tip growth was inhibited. The growth rates of root and side of dendrite arms were improved; therefore, preferential growth of grains was strongly inhibited and as a result, non-dendritic grains occurred during the high grain density solidification process.

4.4 Experimental results

Factors influencing non-dendritic formation in LSPSF processes primarily include pouring temperature, rotative velocity and barrel incline angle. A low pouring temperature benefits the survival of the nuclei formed and separated crystals. The rotative velocity of the barrel determines the level of radial shear and substrate surface for nucleation. The barrel inclination angle determines the component of gravity acceleration parallel to the barrel axis; it also influences the melt flow velocity and axial shear. According to wall mechanisms [27], when melt flows over the barrel, copious nucleation takes place on the barrel wall or in the thermal undercooled region beside the barrel wall. The surface area between the melt and the barrel wall constantly regenerates and offers virtually limitless substrate surface area for nucleation. Hence, new nuclei form on the new surfaces of the barrel wall and undergo the same cycle. When the melt flow and solid movement combine, strong grain movement produces a strong melt flow current. In turn, the strong flow current influences grain movement. In the event of grain movement, grains sinking along the barrel wall induce vortices that influence solid movement and introduce grains into the bulk melt. This dendrite fragmentation theory was postulated by CAMPANELLA et al [28]:

$$C_R = \frac{V}{R} > 1 \tag{18}$$

Their criterion suggested that dendrite fragments detach from growing columnar dendrites and drift towards the center when the magnitude of the interdendritic velocity, V, exceeds the solidification speed (R=D_l/δ). Assuming the flow in the mushy region follows Darcy's law, the magnitude of the interdendritic velocity, V, can be expressed as

$$V = -\frac{K}{f_l \mu}\nabla p \tag{19}$$

where μ is the dynamic viscosity of the liquid, K is the permeability, f_l is the volume fraction of liquid, and p is the dynamic contribution of the pressure responsible for liquid motion in the mushy zone and can be estimated using

$$\|\nabla p\| \approx \rho\left(g\sin\theta_b + \omega^2 r\right) \tag{20}$$

where ρ is the liquid density, θ_b is the barrel incline angle, is the barrel rotative velocity, and r(=0.05 m) is the barrel radius. The permeability term appearing in Eq. (19) comes from the Carman–Kozeny relationship and is given by

$$K = \frac{d_2^2 f_l^3}{180(1-f_l)^2} \tag{21}$$

where d_2 is the secondary dendrite arm spacing (50 μm in this work). Thus, the dendrite fragmentation criterion under the LSPSF is calculated as

$$C_R \approx \frac{\rho(g\sin\theta_b + \omega^2 r)K\delta}{f_l \mu D_l} > 1 \tag{22}$$

Equation (22) shows that increasing the incline angle and rotative velocity of the barrel enhances dendrite fragments; convection carries the fragments from the solidifying front to the inner region of the melt and promotes heterogeneous nucleation. The effects of the axial gravity component exceed the radial inertia force; a larger incline angle benefits dendrite detachment into the mushy region.

The experimental properties and measured physical data of the liquid alloys as well as calculation results of the criterions with LSPSF are given in Table 3. It should be noted that the incline angle of the barrel should be not less than 15° to achieve dendrite fragments; increasing the rotative velocity or the barrel incline angle resulted in abundant dendrite fragments. The strong fluid flow detached the dendrites from the solid–liquid interface and carried them into the bulk melt to form a slurry.

Figure 10(a) clearly shows the microstructures of cast 6063 aluminum alloy without LSPSF and its dendrite character. Figures 10(b−f) show microstructures at a fixed inclined angle (15°) for different rotative velocities (1−2 rad/s). These micrographs show that the microstructures consist primary of α(Al) phases dispersed throughout the alloy matrix; the α(Al) phase became smaller and rounder as the rotative velocity increased and formed globular morphologies. The quantitative results of average particle density and shape factor for the primary α(Al) particles in the semisolid slurries treated with different rotative velocities gradually increased from 120 to 310 mm^{-2} and from 0.46 to 0.59, respectively, as the rotative velocity increased from 1 to 2 rad/s. Compared with the

Table 3 Calculation results of criterions with LSPSF

Parameter	$K/10^{-9}\ m^2$	$\|\|\Delta p\|\|/(N\cdot m^3)$	$R/(10^{-4}\ m\cdot s^{-1})$	f_l	$\mu/(kg\cdot m^{-1}\cdot s^{-1})$	C_R
ω=0 rad/s, θ_b=15°	1.01	5992.1	14.4	0.9	0.0047	0.99
ω=1 rad/s, θ_b=15°	1.01	6110.1	14.2	0.9	0.0047	1.03
ω=2 rad/s, θ_b=15°	1.01	6464.1	14.0	0.9	0.0047	1.10
ω=2 rad/s, θ_b=20°	1.01	8390.3	14.0	0.9	0.0047	1.43
ω=2 rad/s, θ_b=25°	1.01	10256.3	14.0	0.9	0.0047	1.75

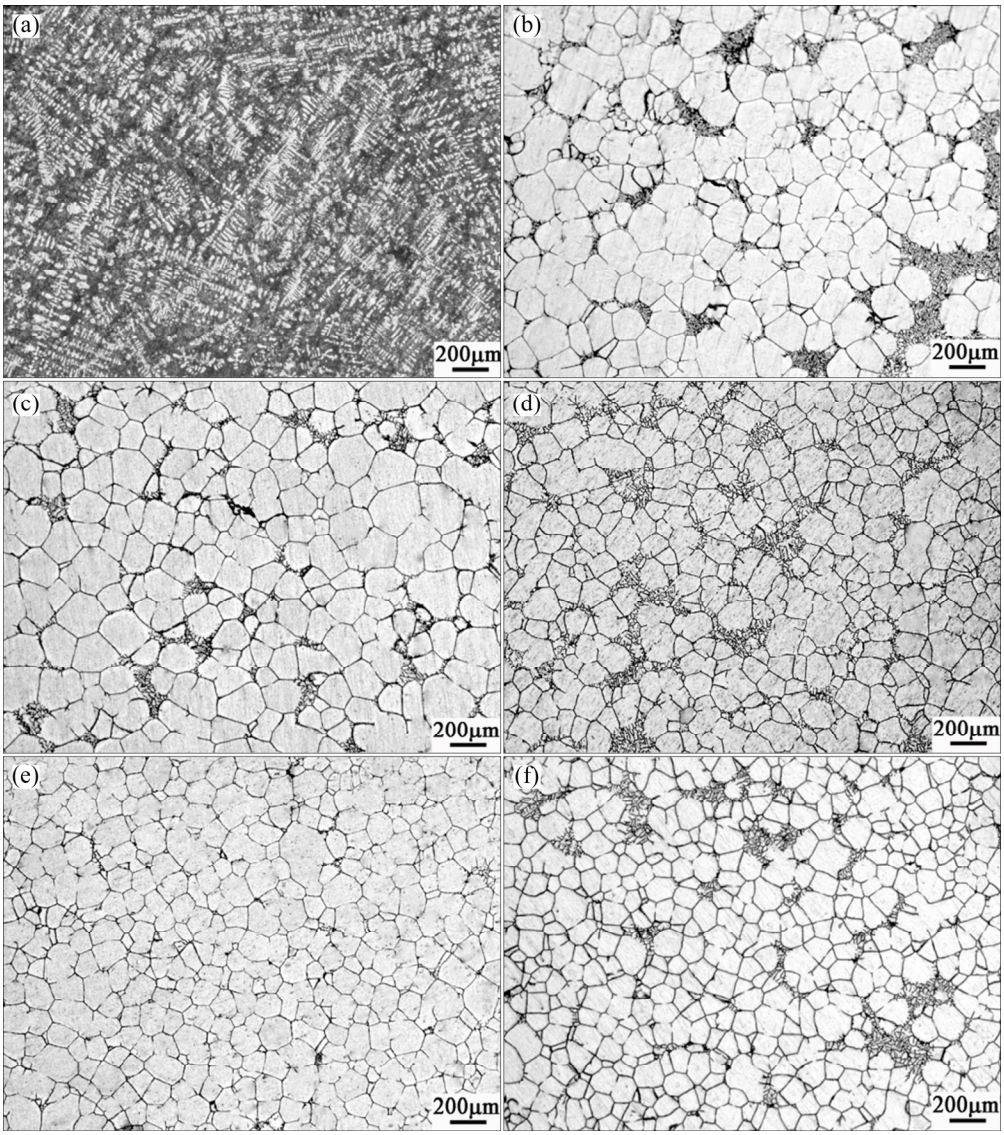

Fig. 10 Microstructures of as-cast 6063 alloy without LSPSF (a) and solidified ingot at fixed inclined angle (15°) with rotative velocities of 1 rad/s (b), 1.25 rad/s (c), 1.5 rad/s (d), 1.75 rad/s (e) and 2 rad/s (f)

simulation results, at low barrel rotation velocities, stirring action of the barrel failed to transfer nucleated grains to the bulk melt effectively. As the barrel rotation velocity increased, the stirring action of the barrel rapidly transferred more nucleated grains to the bulk melt, and thus copious nucleation occurred in a uniform solute and temperature field.

Figure 11 shows the microstructure at a fixed rotative velocity (2 rad/s) for different incline angles (20° and 25°). Both the roundness and grain diameter of the primary α(Al) phase increased as the barrel incline angle increased. The effect of the shear flow intensity also increased as the barrel incline angle increased and resulted in dendrite

motion and increased heat transfer between the melt and the surface of the inclined barrel. These increases all caused additional nucleation. However, when the barrel incline angel exceeded a threshold value, the time of the molten metal on the barrel wall surface dropped, which also lowered shear flow and nucleation. A large incline angle reduced the flow time in the barrel while smaller inclined angle caused a solidified shell within the barrel. Sufficient shear flow and an appropriate time should be selected to obtain a globular primary phase. The f_l should be approximately 0.9 to induce the formation of dendrite fragments and nucleation in the mushy region.

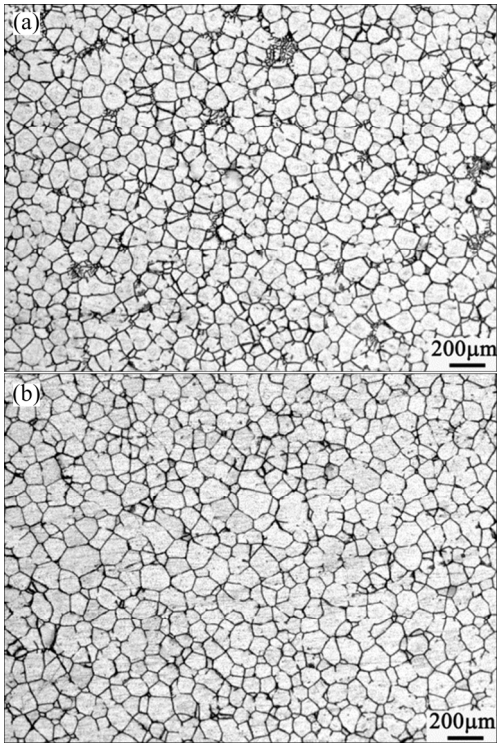

Fig. 11 Microstructures of solidified 6063 at fixed rotative velocity (2 rad/s) for inclined angles of 20° (a) and 25° (b)

5 Conclusions

(1) A phase field lattice Boltzmann model was used to simulate crystal growth and motion under rotation and gravity. LSPSF experiments were conducted to obtain a non-dendritic primary phase. Experimental and simulated results both indicated that finer and rounder semi-solid slurries were obtained at higher rotative velocities. Selecting a suitable inclined angle balanced the flow time and the shear flow intensity in the rotating barrel.

(2) A criterion based on a comparison between the solidification speed and the fluid flow velocity (induced by rotation and gravity) could be applied to LSPSF rheocasting.

(3) It was demonstrated that the phase field lattice Boltzmann model predicted the formation of non-dendritic structures using LSPSF. The next step for the present model is to extend this methodology to examine more complex conditions (such as mechanical vibrations, electromagnetic stirring, and ultrasonic vibrations) and larger-scale poly-crystal multicomponent solidification problems.

References

[1] SPENCER D B, MEHRABIAN R, FLEMINGS M C. Rheological behavior of Sn−15 pct Pb in the crystallization range [J]. Metallurgical and Materials Transactions B, 1972, 3: 1925−1932.

[2] ROJAS R, TAKAKI T, OHNO M. A phase-field-lattice Boltzmann method for modeling motion and growth of a dendrite for binary alloy solidification in the presence of melt convection [J]. Journal of Computational Physics, 2015, 298: 29−40.

[3] GUO Hong-min, YANG Xiang-jie, WANG Jia-xuan, HU Bin, ZHU Guang-lei. Effects of rheoforming on microstructures and mechanical properties of 7075 wrought aluminum alloy [J]. Transactions of Nonferrous Metals Society of China, 2010, 20: 355−360.

[4] LESOULT G. Macrosegregation in steel strands and ingots: Characterisation, formation and consequences [J]. Materials Science and Engineering A, 2005, 413: 19−29.

[5] BOETTINGER W J, WARREN J A, BECKERMANN C, KARMA A. Phase-field simulation of solidification [J]. Annual Review of Materials Research, 2002, 32: 163−194.

[6] ZHU Ming-fang, SUN Dong-ke, PAN Shi-yan, ZHANG Qing-yu, RAABE D. Modelling of dendritic growth during alloy solidification under natural convection [J]. Modelling and Simulation in Materials Science and Engineering, 2014, 22: 034006.

[7] VOLLER V R. An implicit enthalpy solution for phase change problems: With application to a binary alloy solidification [J]. Applied Mathematical Modelling, 1987, 11: 110−116.

[8] TAN L, ZABARAS N. A level set simulation of dendritic solidification with combined features of front-tracking and fixed-domain methods [J]. Journal of Computational Physics, 2006, 211: 36−63.

[9] KARAGADDE S, BHATTACHARYA A, TOMAR G, DUTTA P. A coupled VOF-IBM-enthalpy approach for modeling motion and growth of equiaxed dendrites in a solidifying melt [J]. Journal of Computational Physics, 2012, 231: 3987−4000.

[10] JELINEK B, ESHRAGHI M, FELICELLI S, PETERS J F. Large-scale parallel lattice Boltzmann-cellular automaton model of two-dimensional dendritic growth [J]. Computer Physics Communications, 2014, 185: 939−947.

[11] ZHANG Ang, DU Jing-lian, GUO Zhi-peng, WANG Qi-gui,

XIONG Shou-mei. A phase-field lattice-Boltzmann study on dendritic growth of Al−Cu alloy under convection [J]. Metallurgical and Materials Transactions B, 2018, 49: 3603−3615.
[12] ZHANG Ang, MENG Shao-xing, GUO Zhi-peng, DU Jing-lian, WANG Qi-gui, XIONG Shou-mei. Dendritic growth under natural and forced convection in Al−Cu alloys: From equiaxed to columnar dendrites and from 2D to 3D phase-field simulations [J]. Metallurgical and Materials Transactions B, 2019, 50: 1514−1526.
[13] ZHANG X, KANG J, GUO Z, XIONG S, HAN Q. Development of a Para-AMR algorithm for simulating dendrite growth under convection using a phase-field-lattice Boltzmann method [J]. Computer Physics Communications, 2018, 223: 18−27.
[14] LIU L, PIAN S, ZHANG Z, BAO Y, LI R, CHEN H. A cellular automaton-lattice Boltzmann method for modeling growth and settlement of the dendrites for Al−4.7%Cu solidification [J]. Computational Materials Science, 2018, 146: 9−17.
[15] MEDVEDEV D, VARNIK F, STEINBACH I. Simulating mobile dendrites in a flow [J]. Procedia Computer Science, 2013, 18: 2512−2520.
[16] TAKAKI T, SATO R, ROJAS R, OHNO M, SHIBUTA Y. Phase-field lattice Boltzmann simulations of multiple dendrite growth with motion, collision, and coalescence and subsequent grain growth [J]. Computational Materials Science, 2018, 147: 124−131.
[17] KARMA A. Phase-field formulation for quantitative modeling of alloy solidification [J]. Physical Review Letters, 2001, 87: 115701.
[18] ECHEBARRIA B, FOLCH R, KARMA A, PLAPP M. Quantitative phase-field model of alloy solidification [J]. Physical Review E, 2004, 70: 061604.
[19] BECKERMANN C, DIEPERS H J, STEINBACH I, KARMA A, TONG X. Modeling melt convection in phase-field simulations of solidification [J]. Journal of Computational Physics, 1999, 154: 468−496.
[20] GLOWINSKI R, PAN T W, HESLA T I, JOSEPH D D, PÉRIAUX J. A fictitious domain approach to the direct numerical simulation of incompressible viscous flow past moving rigid bodies: Application to particulate flow [J]. Journal of Computational Physics, 2001, 169: 363−426.
[21] FENG Zhi-gang, MICHAELIDES E E. The immersed boundary-lattice Boltzmann method for solving fluid-particles interaction problems [J]. Journal of Computational Physics, 2004, 195: 602−628.
[22] JACOT A, RAPPAZ M. A pseudo-front tracking technique for the modelling of solidification microstructures in multi-component alloys [J]. Acta Materialia, 2002, 50: 1909−1926.
[23] GENG Shao-ning, JIANG Ping, SHAO Xin-yu, MI Gao-yang, WU Han, AI Yue-wei, WANG Chun-ming, HAN Chu, CHEN Rong, LIU Wei. Comparison of solidification cracking susceptibility between Al−Mg and Al−Cu alloys during welding: A phase-field study [J]. Scripta Materialia, 2018, 150: 120−124.
[24] BOGNO A, NGUYEN-THI H, REINHART G, BILLIA B, BARUCHEL J. Growth and interaction of dendritic equiaxed grains: In situ characterization by synchrotron X-ray radiography [J]. Acta Materialia, 2013, 61: 1303−1315.
[25] TÖNHARDT R, AMBERG G. Dendritic growth of randomly oriented nuclei in a shear flow [J]. Journal of Crystal Growth, 2000, 213: 161−187.
[26] GUO Hong-min, YANG Xiang-jie. Formation mechanism of spherical particles in undercooled melt [J]. The Chinese Journal of Nonferrous Metals, 2008, 18: 651−659. (in Chinese)
[27] HUTT J, STJOHN D. The origins of the equiaxed zone−Review of theoretical and experimental work [J]. International Journal of Cast Metals Research, 1998, 11: 13−22.
[28] CAMPANELLA T, CHARBON C, RAPPAZ M. Grain refinement induced by electromagnetic stirring: A dendrite fragmentation criterion [J]. Metallurgical and Materials Transactions A, 2004, 35: 3201−3210.

基于相场格子玻尔兹曼模型的铝合金 LSPSF 非枝晶形成

吁安山[1,2]，杨湘杰[1,2]，郭洪民[2,3]

1. 南昌大学 机电工程学院，南昌 330031；
2. 江西省高性能精确成形重点实验室，南昌 330031；
3. 南昌大学 材料科学与工程学院，南昌 330031

摘 要：采用数值模拟研究基于低过热度剪切制浆机铝合金凝固初期非枝晶组织的形成。采用格子玻尔兹曼法和相场法相结合，模拟枝晶在凝固过程中的生长和运动。模拟结果表明，充分的剪切流有助于浓度场的均匀化、晶体的旋转和非枝晶的形成。讨论晶粒间的相互作用。在枝晶臂部分重熔的基础上，建立 LSPSF 枝晶断裂判据，发现强剪切流和较大的倾斜角度能够增强枝晶断裂，并对模拟结果进行实验验证。

关键词：数值模拟；非枝晶组织；低过热度剪切制浆(LSPSF)；铝合金；相场法；格子玻尔兹曼法

(Edited by Bing YANG)